Modeling and Experiments on Flexible Side-Electrodes Electrostatic Actuators: Influence of the Contact Interface on the Available Force

Patrice Le Moal, Gilles Bourbon

Univ. Bourgogne Franche-Comté, FEMTO-ST Institute, CNRS/UFC/ENSMM/UTBM, Department of Applied Mechanics, France

*Corresponding author Patrice Le Moal: Département Mécanique Appliquée, 24 rue de l'épitaphe 25000 Besançon, France

E-mail address: patrice.lemoal@femto-st.fr

Keywords: flexible side-electrodes electrostatic actuators, useful force, analytical modeling, experimental characterization, residual air thickness

Abstract:

This paper presents an in-depth study of electrostatic actuators based on flexible side-electrodes focusing on the available electrostatic force and the derived useful force. A design tool is proposed considering technological aspects as aspect ratio, insulating layer material and voltage level.

A space discretized mechanical approach based on Euler-Bernoulli beam theory is developed to model the bending deflection of the flexible movable electrode and "zipping" contact. Analytical developments and simplifications are achieved, rapidly and efficiently implemented in a proposed algorithm. ANSYS® simulations validate the procedure for updating the contact zone through the updating of the electrostatic pressure distribution. Optimum movable electrode width and appropriate "opposable" stiffness for guiding system are discussed. A "residual air thickness" parameter is introduced to address imperfect contact between the electrodes.

Experimental characterization studies various prototypes with different structural parameters as thickness (50µm and 200µm), gaps (5µm and 15µm) and material for insulating layers (silicon oxide and parylene C). The metrology campaign highlights the impact of aspect ratio and oxidation/deoxidation on electrode sidewall quality and hence mechanical performance.

A comparison with well-known comb-drive shows higher electrostatic force for flexible side-electrode actuators. As an example, for a 10µm stroke, the available electrostatic force for flexible electrodes with irregular sidewalls (residual air thickness 0.6µm) is 2.2 times greater and rises to 7.3 times greater for perfect sidewalls (no residual air).

1. Introduction

Electrostatic interactions are commonly involved in many microelectromechanical systems (MEMS) as sensors or actuators due to the abilities of MEMS-based technologies to achieve micrometer gaps. In the case of sensors as accelerometers [1, 2], micrometer gaps allow the sensitivity to be increased. On the other hand, electrostatic actuators are widely used thanks to their high energy densities and forces mainly in positioning applications [3, 4].

Electrostatically actuated microsystems come in a variety of forms in two main configurations depending on applications. For RF switches [5, 6, 7], parallel plate configuration is often preferred mainly because of their simplicity of design and very high holding forces in the contact position. Parallel plate configuration is well adapted to low stroke applications. For micro grippers [8, 9], optical devices [10, 11] or positioning/motor applications [12, 13, 14, 15], parallel plate or comb-drive configurations are chosen according to the displacement and force specifications, the available footprint, or manufacturing requirements.

Parallel plate and comb-drive configurations involve respectively two basic force concepts [16], normal forces to actuate closing gap actuators and tangential forces to actuate overlapping electrode actuators. Comb-drive configurations are characterized by a constant electrostatic force along the stroke that is interesting from a control perspective. However, guiding systems induce an opposite elastic force generally proportional to displacement and therefore reduce the useful force along the stroke. In addition, special care must be taken with guiding systems, as transverse instability can lead to short-circuiting or breakage of interdigitated combs. The parallel plate configuration is less sensitive to guiding system stiffness, as the electrostatic force increases during displacement. On the other hand, the stroke is often reduced, as gaps of a few micrometers are needed to involve a relevant electrostatic pressure.

To achieve larger displacements from a few tens to a hundred micrometers with a parallel plate configuration, the use of a flexible electrode is introduced in particular by Legtenberg et al [17]. The mechanism of progressive contact between flexible movable and rigid fixed electrodes is known as “zipping”. As proposed by Li et al [18] and Burugupally [19], the concept of a flexible movable electrode is often associated with a curved fixed electrode to maximize displacement. In the above designs, the movable flexible electrode is clamped at one end and the displacement can be transferred to an external element at the opposite free end. Therefore, curved fixed electrodes are designed with small gaps on the clamped end and larger gaps on the free end. Moreover, Li et al [18] add to the curved fixed electrode a flexible thinner part at the starting zone in order to make easier the initiation of zipping. Hoffmann et al [20] proposes another architecture for a switch application. The movable

structure consists of two connected beams: the first beam acts as the flexible electrode and the second beam as a spring linked to the rigid support. In particular, the authors studied the influence of the relative stiffness of the two beams on the mechanical behavior of the assembly.

The architecture of electrostatic actuator proposed in this work is similar to that of Hoffmann [20]. However, it is here intended to be applied to motorization and aims at generating a relevant useful force. Several movable flexible electrodes are connected to a shuttle at one end for the force/displacement transfer and free at the other end to initiate zipping against fixed straight electrodes.

Different modeling approaches have been investigated to develop design tools. Legtenberg et al [17] proposed a two-dimensional quasi-static model based on analytical energy methods assuming polynomial deflection profile which coefficients are numerically identified. Li et al [18] and in more detail Li [21] described a numerical solution in MATLAB® of the Euler-Bernoulli equation according to the “before pull-in” and “after pull-in” phases. Also based on the Euler-Bernoulli equation in its forms describing the local curvature, Oberhammer et al [22] presents a quasi-static space discretized model. The resolution algorithm relies on the calculation of the electrostatic pressure distribution and the successive integrations to get bending moments, rotations and finally displacements. Many works [17, 19, 21] include finite element simulations with commercial softwares but their time-consuming nature does not make them suitable as a design tool, and they are considered more as a validation step in the final dimensioning phase.

The present work deals with an in-depth study of actuators based on flexible side-electrodes from theory to experiment including the influence of the contact interface on mechanical performance. In the current context, these actuators are primarily designed for positioning and motor applications such as watch hands, valves, shutters, and so on …. Therefore, available electrostatic force and useful force are of particular interest. The targeted applications include stepper driving of gear wheels or trains, for instance, using a pawl and ratchet system. The elementary displacement is determined by the electrostatic gap which is supposed to be closed at each actuation step. Such a driving mechanism minimizes the holding contact time of zipping electrodes which is beneficial for addressing common reliability and durability issues associated with zipper actuators. In Section 2, the specific capabilities of three types of electrostatic actuators are compared in terms of available electrostatic force and useful force. The analytical modeling presented in Section 3 adopts a quasi-static, two-dimensional approach based on the Euler-Bernoulli beam theory, similar to the method proposed by Oberhammer et al. [22]. Analytical developments are carried out, and an efficient solution algorithm is proposed to characterize the zipping mechanism and in particular the available electrostatic force. Model results and the underlying assumptions are validated through numerical simulations using ANSYS®. Design

considerations regarding an optimum electrode width and an "opposable" guiding stiffness are proposed in light of the available electrostatic force and the useful force. Section 4 aims to experimentally test the model in terms of available electrostatic force. For this purpose, experimental investigations are conducted including different combinations of fabrication (called "set-ups") based on Deep Reaction Ion Etching of SOI (Silicon on Insulator), metrology and force characterizations. A close relationship between available electrostatic force and nature of the contact interface is established from the "residual air thickness" reflecting roughness and non-verticality of sidewalls. Lastly, section 5 gives conclusions and perspectives.

2. Actuators based on Flexible Side-Electrodes (*AFSE*): electrostatic and useful force capabilities

2.1. Architectures of AFSE, ARSE and ARIC

Figure 1 shows the schematic architecture of three types of electrostatic actuators devoted to motorization. These actuators are configured so as, for example, to drive a toothed element (wheel or rack, schematically represented in black on Figure 1) as in the applications described in [12].

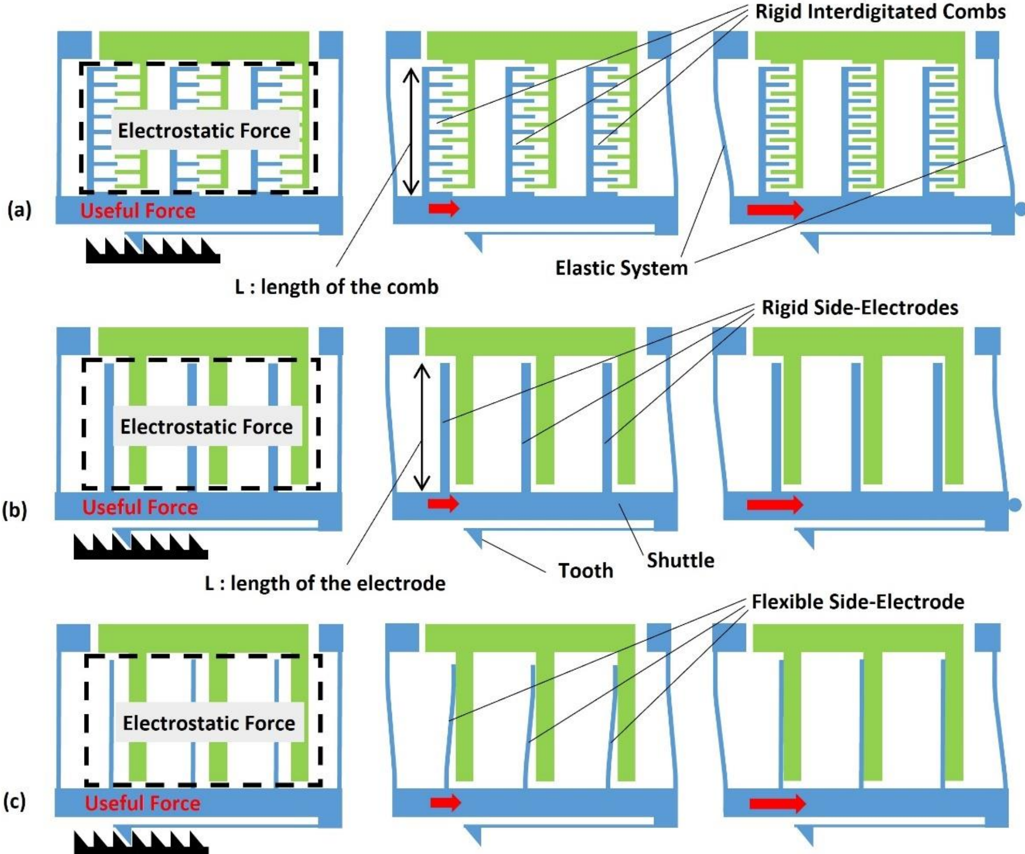

Figure 1: Schematic architectures of electrostatic devoted to motorization: Actuators base on Rigid Interdigitated Combs (ARIC, Fig. 1a), Actuators based on Rigid Side-Electrodes (ARSE, Fig. 1b) and Actuators based on Flexible Side-Electrodes (AFSE, Fig. 1c)

The three actuators are composed of fixed electrodes (green) linked to the substrate, and movable electrodes (blue) linked to the substrate by an elastic system. The movable electrodes are attached to a shuttle/tooth (blue) unit to which displacement and force can be transmitted. The driving stage, in the red arrow direction in Figure 1, is generated by electrostatic interactions between fixed and movable electrodes respectively connected to a given voltage V and the ground. These electrostatic interactions take place within the dashed black rectangle in Figure 1 and give rise to the resultant electrostatic force. This force is generated either through interdigitated combs or rigid/flexible electrodes depending on the type of actuator being used. The return to the initial position is achieved thanks to elastic restoring force of the guiding beams. To assess the specific capabilities of these actuators for motor applications, two types of force are distinguished in relation to the resultant electrostatic force:

- the available electrostatic force: this refers to the electrostatic force that can be transmitted to the shuttle from the resultant electrostatic force. That corresponds in practice to the mechanical reaction of the shuttle when it is assumed to be blocked in the displacement direction.
- and the useful force: this denotes the force that can be transmitted to an external element from the shuttle/tooth unit. It is the available electrostatic force reduced by the elastic restoring force of the guiding system. For example, the external element could be a gear wheel/train responsible for driving any subsequent load.

2.2. Available electrostatic force of AFSE, ARSE and ARIC

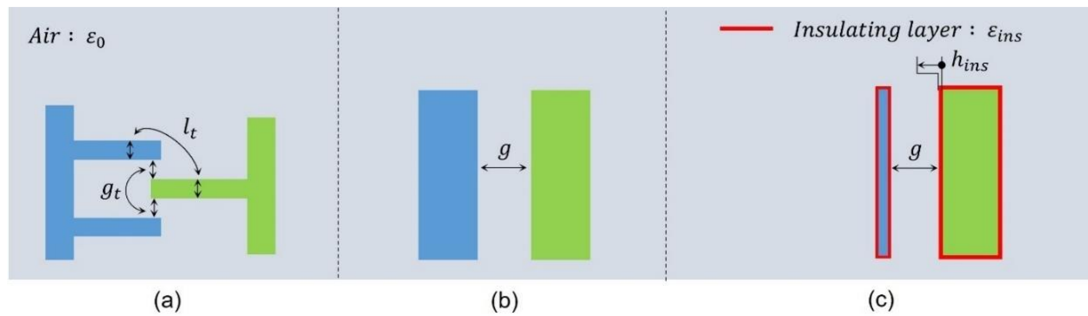

Figure 2: Geometric parameters of the electrostatic interactions of ARIC (a), ARSE (b) and AFSE (c)

For *ARIC* (Figures 1a/2a) and *ARSE* (Figures 1b/2b), combs or electrodes are only connected to the shuttle and no contact takes place. Therefore, available electrostatic force and resultant electrostatic force are identical and they are expressed as functions of the shuttle's displacement Δ as follows:

$$F_{ARIC}(\Delta) = \frac{\varepsilon_0 b U^2}{2 g_t} \times 2N = \frac{\varepsilon_0 b L U^2}{2 g_t (l_t + g_t)} = Constant \quad ; \quad F_{ARSE}(\Delta) = \frac{\varepsilon_0 b L U^2}{2(g - \Delta)^2} \qquad \text{(1-2)}$$

with $\varepsilon_0 = 8.854.10^{-12}\,F/m$ the permittivity of air, b the structural thickness (thickness of the device layer in the SOI wafer), U the applied voltage, *2N* the number of electrostatic interactions, g_t, g *and* l_t respectively tangential/normal gaps and width of comb teeth (shown in Figure 2) and L the length of the comb/electrode (Figure 1). Expressions (1-2) consider for *ARIC* that *N* teeth are uniformly distributed along the electrode length *L* and for *ARSE* that the overlapped lengths of fixed and movable electrodes are very close to the total length *L*. In both cases *ARIC* and *ARSE*, combs and electrodes are supposed to be rigid and designed to be so. No insulating layer is required due to an end stop preventing short-circuits (blue disk in Figure 1).

For *AFSE* (Figures 1c/2c), movable electrodes are assumed to be flexible. By zipping, it is possible to exploit smaller gaps and amplify electrostatic interactions. Due to the contact operating principle, an insulating layer must be deposited on the sides of the fixed and movable electrodes. However, available electrostatic force and resultant electrostatic force are not identical since a contact point or area appears on the free end of the movable electrode. Thus, identification of the mechanical reaction of the shuttle when it is assumed to be blocked requires modeling the progressive contact between fixed and movable electrodes, as detailed in Section 3. Eq. (3) provides the total resultant electrostatic force including "motor" and "contact" components and specifies the parameters involved:

$$F_{AFSE}^{resultant} = \int_0^L \frac{\varepsilon_0 \varepsilon_{ins}^2 b U^2}{2\left[\left(g - \Delta + z(x)\right)\varepsilon_{ins} + 2h_{ins}\varepsilon_0\right]^2} dx \qquad with\ z(x) \leq 0 \tag{3}$$

with ε_{ins} and h_{ins} respectively the permittivity and the thickness of the insulation layer, x the position varying from the shuttle/electrode connection ($x = 0$) to the electrode free end ($x = L$) and $z(x)$ the bending deflection of the flexible electrode.

The analytical-numerical procedure described in Section III and equations (1-2) are used to draw up Figure 3 and compare the available electrostatic force at start, i.e., $\Delta = 0$.

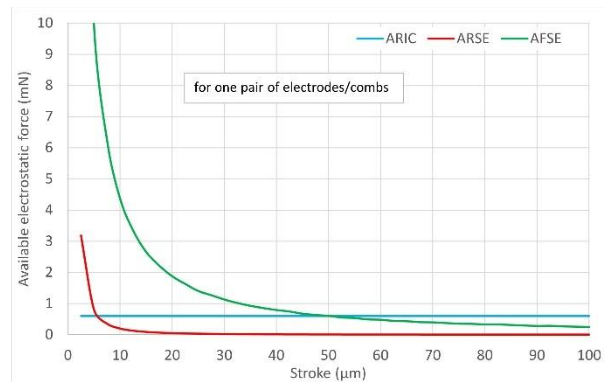

Figure 3: Theoretical available electrostatic force (at $\Delta = 0$*) as a function of the stroke for ARIC, ARSE and AFSE -* $\varepsilon_{ins} = 3.9 \times\ \varepsilon_0; L_{c/e} = 1000\mu m; g_t = 3.5\mu m; b = 200\mu m; l_t = 6\mu m; h_{ins} = 0.4\mu m; U = 150V$

Figure 3 illustrates that *AFSE* outperforms *ARSE* regardless of the stroke. When comparing *AFSE* and *ARIC*, *AFSE* is superior if strokes are less than 50µm. Additional simulations show that the forces ratios are maintained for different lengths of electrodes and voltages.

2.3. Useful force of AFSE and ARIC

Assuming that the elastic restoring forces of guiding beams are linear, the useful force is:

$$F_{useful}(\Delta) = F_{available}(\Delta) - k_{guiding}\Delta \tag{4}$$

with $k_{guiding}$ the bending stiffness of the guiding beams.

Considering that an actuator must drive its opposing load throughout its stroke, the true potential in terms of useful force is its minimal value during the stroke. Thus, according to Eq. (4), a maximum value of this potential is the available electrostatic force at 0 displacement, i.e.: $F_{available}(0)$.

Let's consider two actuators *ARIC* and *AFSE* with 10 pairs of combs/electrodes and a stroke of 50µm. The elastic system composed of two guiding beams with length/width/thickness equal to 1000µm/10µm/200µm is characterized by a bending stiffness around 67.6N/m. Figures 4 highlight a specific advantage of *AFSE* over *ARIC* due to the increasing available electrostatic force as the shuttle moves. If both *AFSE* and *ARIC* induces $F_{available}(0) \approx 6.1mN$, the useful force along the stroke increases for *AFSE* and drastically falls by 56% for *ARIC*. This enables the design of an elastic guiding system that is sufficiently rigid to impart robustness to the device; particularly in terms of dynamic behavior by filtering out rigid body modes of the shuttle at higher frequencies. Furthermore, this prevents stiction issues by facilitating the removal of flexible electrode as the voltage drops to zero.

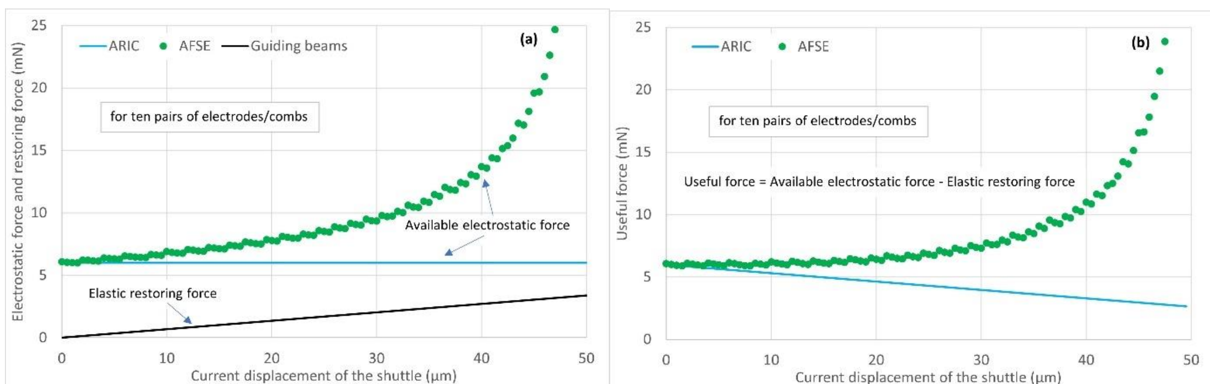

Figure 4: Theoretical evolution of the electrostatic (a) and useful (b) forces throughout the shuttle displacement at 150V in the case of ARIC and AFSE, with 10 pairs of electrodes/combs and a stroke of 50µm

3. Analytical/numerical modeling of the electromechanical energy transduction at the interface of flexible movable/rigid fixed side-electrode and design considerations

3.1. Formalism and resolution of bending behavior without any contact

This part deals with a simpler problem than this including contact but allows the formalism chosen to be clearly exposed. Figure 5 presents the equilibrium of a movable electrode subjected to the electrostatic pressure $p_{elec}(x) = \frac{F^{L}_{AFSE}}{b}(Eq.3)$ with any boundary conditions. Edge effects are assumed to be negligible and not considered in Equation (2). The electrostatic pressure is linearized in accordance with a space discretized formalism as in [22]:

$$p_j(x) = p_j + \frac{(p_{j+1} - p_j)}{(x_{j+1} - x_j)}(x - x_j) \quad \forall x \in [x_j, x_{j+1}] \; and\; for\; j \in \{1,2, \dots, n\} \tag{5}$$

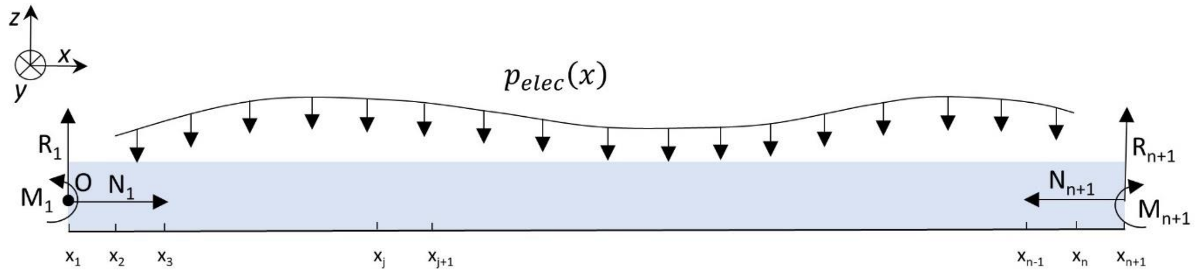

Figure 5: Equilibrium of a movable electrode under an electrostatic pressure p(x)

The balance of forces and moments in relation to point O (Figure 5) gives:

$$\begin{cases} N_1 = N_{n+1}\; (not\; used) \\ R_1 + R_{n+1} = F_{tot} \\ -M_{n+1} + M_1 + R_{n+1}L = M_{tot} \end{cases} \quad \text{with} \quad \begin{cases} F_{tot} = \int_0^L p_{elec}(x)dx \\ M_{tot} = \int_0^L p_{elec}(x)xdx \end{cases} \tag{6}$$

According to Euler-Bernoulli beam theory (implying the need to satisfy small width-to-length and deflection-to-length ratios [22]), the curvature of the electrode $\ddot{z}(x)$ (with $z(x)$ the bending deflection of electrode) is defined by:

$$\ddot{z}(x) = \frac{-M_{elec}(x) - M_{n+1} + R_{n+1}(L - x)}{EI} \tag{7}$$

with: $M_{elec}(x) = \int_x^L p_{elec}(u)(u - x)du$

with E the modulus of Young, I the moment of inertia about the y-axis. By integrating equation (7) two times, rotation $\dot{z}(x)$ and bending deflection $z(x)$ are defined for $x \in [x_j, x_{j+1}]_{j\in\{1,\dots,n\}}$ by:

$$\begin{cases} \dot{z}_j(x) = \frac{1}{EI}\left[T_j(x) - M_{n+1}x + R_{n+1}\left(Lx - \frac{x^2}{2}\right)\right] + C_{2j-1} \\ z_j(x) = \frac{1}{EI}\left[U_j(x) - M_{n+1}\frac{x^2}{2} + R_{n+1}\left(L\frac{x^2}{2} - \frac{x^3}{6}\right)\right] + C_{2j-1}x + C_{2j} \end{cases} \tag{8}$$

Analytical expressions of $M_{elec}(x), F_{tot}, M_{tot}, T_j(x)$ and $U_j(x)$ are reported in Appendix.

The constants $C_{j\in\{1,\ldots,2n\}}$ are determined by the boundary and continuity conditions:

- Assuming elastic supports characterized by longitudinal k_l^1 and k_l^{n+1} and torsional k_t^1 and k_t^{n+1} stiffnesses, boundary conditions can be written: $z_1(0) = -R_1/k_l^1$, $\dot{z}_1(0) = -M_1/k_t^1$, $z_{n+1}(L_e) = -R_{n+1}/k_l^{n+1}$, $\dot{z}_{n+1}(L_e) = M_{n+1}/k_t^{n+1}$.
- Continuity conditions express the continuity of rotation and displacements at the bounds of the intervals $[x_j, x_{j+1}]_{j\in\{1,\ldots,n\}}$, i.e.: $\dot{z}_j(x_{j+1}) = \dot{z}_{j+1}(x_{j+1})$ and $z_j(x_{j+1}) = z_{j+1}(x_{j+1})$

Using Equations (6) and (8) with boundary and continuity conditions gives the *(2n+4)* equations of the system (9) (AF_j and AG_j introduced to simplify writing the equations are reported in Appendix):

$$\begin{cases} R_1 + R_{n+1} = F_{tot} \\ R_{n+1}L + M_1 - M_{n+1} = M_{tot} \\ \dfrac{M_1}{k_t^1} + C_1 = -\dfrac{1}{EI}p_1\dfrac{x_2^3}{6} \\ \dfrac{R_1}{k_l^1} + C_2 = \dfrac{1}{EI}p_1\dfrac{x_2^4}{24} \\ \dfrac{1}{EI}\dfrac{L^2}{2}R_{n+1} + M_{n+1}\left(-\dfrac{L}{EI} - \dfrac{1}{k_t^{n+1}}\right) + C_{2n-1} = -\dfrac{1}{EI}T_n(x_{n+1}) \\ R_{n+1}\left(\dfrac{1}{EI}\dfrac{L^3}{3} + \dfrac{1}{k_l^{n+1}}\right) - \dfrac{1}{EI}\dfrac{L^2}{2}M_{n+1} + C_{2n-1}L + C_{2n} = -\dfrac{1}{EI}U_n(x_{n+1}) \\ C_{2j+1} - C_{2j-1} = AF_j \quad (j \in \{1,2,\ldots,n-1\}) \\ C_{2j+2} - C_{2j} = AG_j - AF_j x_{j+1} \quad (j \in \{1,2,\ldots,n-1\}) \end{cases} \tag{9}$$

Solution of the linear system (9) requires the inversion of a *(2n+4) x (2n+4)* matrix that can be time-consuming. By eliminating the constants $C_{j\in\{1,\ldots,2n\}}$, solution of system (9) is equivalent to solving the reduced *4 x 4* following system (10):

$$\begin{cases} R_1 + R_{n+1} = F_{tot} \\ R_{n+1}L + M_1 - M_{n+1} = M_{tot} \\ R_{n+1}\left(-\dfrac{1}{EI}\dfrac{L^2}{2}\right) + \dfrac{M_1}{k_t^1} + M_{n+1}\left(\dfrac{L}{EI} + \dfrac{1}{k_t^{n+1}}\right) \\ \quad = -\dfrac{1}{EI}p_1\dfrac{x_2^3}{6} + \dfrac{1}{EI}T_n(x_{n+1}) + \displaystyle\sum_{j=1}^{j=n-1} AF_j \\ \dfrac{R_1}{k_l^1} + R_{n+1}\left(\dfrac{1}{EI}\dfrac{L^3}{6} - \dfrac{1}{k_l^{n+1}}\right) + M_{n+1}\left(-\dfrac{1}{EI}\dfrac{L^2}{2} - \dfrac{L}{k_t^{n+1}}\right) \\ = \dfrac{1}{EI}U_n(x_{n+1}) + \dfrac{1}{EI}p_1\dfrac{x_2^4}{24} + \displaystyle\sum_{j=1}^{j=n-1}\left(AG_j - x_{j+1}AF_j\right) - \dfrac{1}{EI}T_n(x_{n+1})L \end{cases} \tag{10}$$

Thus, bending behavior without any contact is solved according to the following process:

- Unknowns R_1, R_{n+1}, M_1 and M_{n+1} are calculated by resolution of system (10),
- Calculations of $C_1 = -p_1 x_2^3/6EI - M_1/k_t^1$; $C_2 = p_1 x_2^4/24EI - R_1/k_l^1$ and other constants C_j ($j \in \{3, \ldots, 2n\}$) are progressively identified by two last equations of system (9),
- Finally, rotation $\dot{z}_j(x)$ and displacement $z_j(x)$ are given by (8).

3.2. Bending behavior with contact

For *AFSE*, $R_{n+1} = M_{n+1} = 0$ at the free end before contact (No contact solution in Figure 7). When contact occurs and spreads, additional reactions from the fixed electrode $R_{n-p+2}, R_{n-p+3}, \ldots, R_n, R_{n+1}$ are introduced corresponding to *p* contact points (See Figure 6) preventing the interpenetration of electrodes. For each contact point, the bending deflection is also set to the normal gap $-g$.

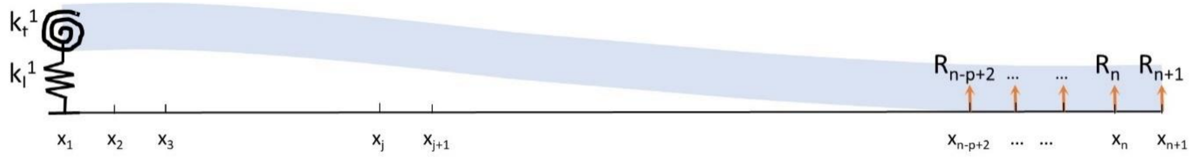

Figure 6: Image of the deformed electrode with p points of contact: additional reactions (R_i) are introduced

The bending moment at a section located at *x* depends on the *j*^th interval considered as follows:

$$\begin{cases} M_f = -M_{elec}(x) + \sum_{k=n-p+2}^{k=n+1} R_k(L - \delta(n+1-k) - x) & j \in \{1, \ldots, n-p+1\} \\ M_f = -M_{elec}(x) + \sum_{k=j+1}^{k=n+1} R_k(L - \delta(n+1-k) - x) & j \in \{n-p+2, \ldots, n\} \end{cases} \quad (11)$$

with : $\delta = \frac{L}{n}$. Given the form of the bending moment, continuity conditions depend on the considered interval, for $j \in \{1, \ldots, n-p\}$, $\boldsymbol{\alpha} = \mathbf{0}$, and for $j \in \{n-p+1, \ldots, n-1\}$, $\boldsymbol{\alpha} = \mathbf{1}$:

$$, \begin{cases} C_{2j+1} = C_{2j-1} + \boldsymbol{\alpha} \frac{1}{EI} R_{j+1} \left(\left(L - \delta(n-j) \right) x_{j+1} - \frac{x_{j+1}^2}{2} \right) + AF_j \\ C_{2j+2} = C_{2j} + \boldsymbol{\alpha} \frac{1}{EI} R_{j+1} \left(-\left(L - \delta(n-j) \right) \frac{x_{j+1}^2}{2} + \frac{x_{j+1}^3}{3} \right) + AG_j - x_{j+1} AF_j \end{cases} \quad (12)$$

The resulting system including the new equilibrium equations, boundary and continuity equations would consist of *(2n+p+2)* unknowns and equations with $p \in \{1, \ldots, n+1\}$. As in the no-contact study, the solution system is reduced to a *(p+2) x (p+2)* system with R_1, M_1, R_{n-p+2} to R_{n+1} as unknowns:

$$
\begin{cases}
R_1 + \sum_{j=n-p+2}^{j=n+1} R_j = F_{tot} \\
\sum_{j=n-p+2}^{j=n+1} R_j\big(L - \delta(n+1-j)\big) + M_1 = M_{tot} \\
-\frac{M_1}{k_t^1} x_{j+1} - \frac{R_1}{k_l^1} + \frac{1}{EI} \sum_{k=n-p+1}^{k=n} R_k \left([L - \delta(n-k)] \frac{x_{j+1}^2}{2} - \frac{x_{j+1}^3}{6} \right) = -g \\
+\frac{1}{EI} p_1 \frac{x_2^3}{6} x_{j+1} - \frac{1}{EI} p_1 \frac{x_2^4}{24} - \frac{1}{EI} U_j\big(x_{j+1}\big) - \sum_{k=1}^{k=j-1} AF_k\, x_{j+1} - \sum_{k=1}^{k=j-1} (AG_k - x_{k+1} AF_k) \\
for\ j \epsilon \{n-p+1, \dots, n\}
\end{cases}
\tag{13}
$$

Solution of (13) and calculations of constants $C_j, j \in \{1, \dots, 2n\}$ allow to access the displacement by the following system (14) according to the jth interval:

$$
z_j(x) = C_{2j-1}x + C_{2j} + \tfrac{1}{EI} U_j(x) +
$$
$$
+ \begin{cases}
\frac{1}{EI} \sum_{k=n-p+2}^{k=n+1} R_k \left([L - \delta(n-k+1)] \frac{x^2}{2} - \frac{x^3}{6} \right) & if\ j \in \{1, \dots, n-p+1\} \\
\frac{1}{EI} \sum_{k=j+1}^{k=n+1} R_k \left([L - \delta(n-k+1)] \frac{x^2}{2} - \frac{x^3}{6} \right) & if\ j \in \{n-p+2, \dots, n\}
\end{cases}
\tag{14}
$$

The progressive contact between a movable flexible electrode and a fixed rigid one can be solved according to the algorithm proposed in Figure 7. Iterations are conducted on the displacement determination to take into account updating of the electrostatic pressure distribution depending on the deflection. A stopping criterion defines the stabilization obtained between two successive iterations. The available electrostatic force, that can be transferred to the shuttle, is given by the reaction R_1 considering an “infinite" value of the longitudinal stiffness (in practice, about $k_l^1 = 10^{20} N/m$). Its evolution along the stroke is obtained by progressively reducing the initial gap and solving the algorithm in Figure 7.

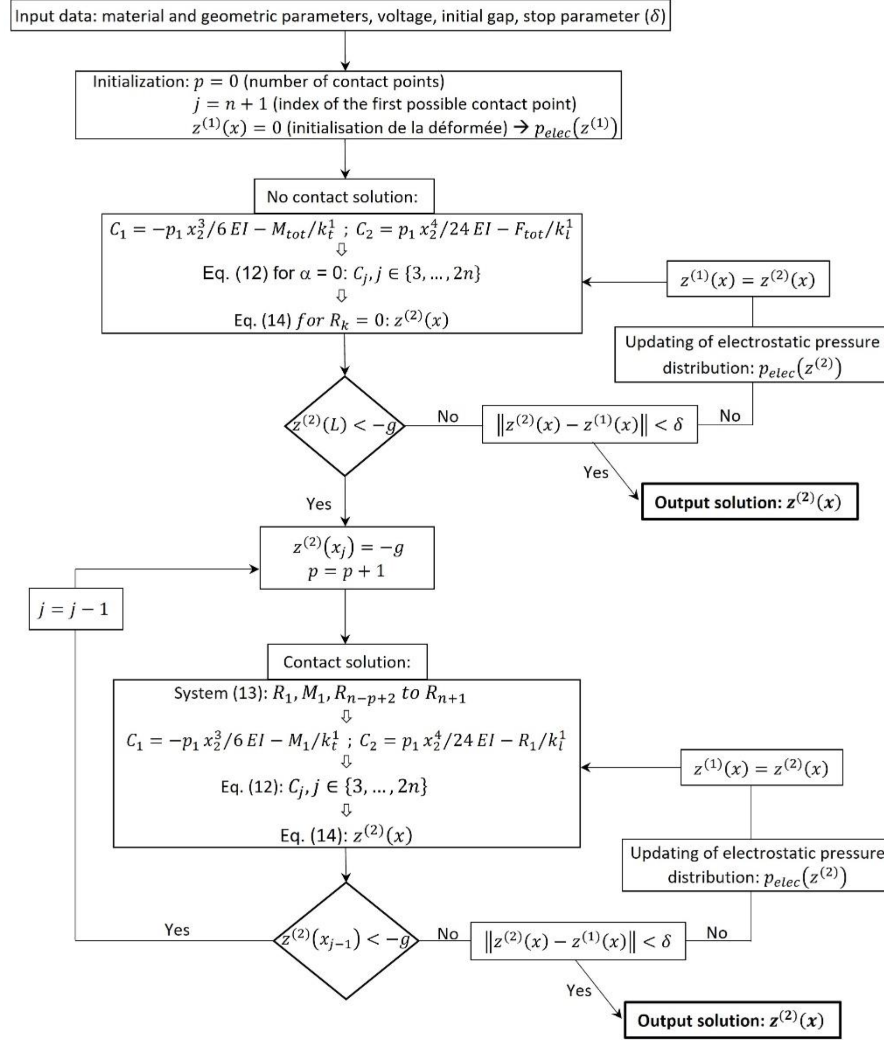

Figure 7: Algorithm outlining the solution for progressive contact between a flexible electrode and a rigid one

3.3. *Model results and finite element calculations with ANSYS®: toward design considerations*

The validation configuration in ANSYS® is composed of a beam with a free-clamped boundary condition. PLANE183 solid elements (2D-8-node elements) mesh the flexible electrode and TRANS126 electromechanical elements mesh the dielectric gap acting as a capacitive transducer. Moreover, TRANS126 includes contact abilities and allows a dielectric multilayer to be considered. ANSYS® simulations take into account a more general mechanical behavior encompassing in particular shear and geometric non-linearities. Consequently, the validation of model results through ANSYS® simulations will support the Euler-Bernoulli assumptions made in the conducted simulations. In practice, for expected voltage values below 200V, the fundamental zipping mechanism necessitates the selection of small width-to-length and deflection-to-length ratios generally satisfying the Euler-Bernoulli assumptions.

<u>About the deflection shape and the contact area: “zipping” configurations</u>

Figures 8 illustrate the deflection shape at 150V for two examples of flexible electrodes and the corresponding contact area. Validation of the present model is clearly established by an excellent correlation with ANSYS® results for 2 values of electrode width and 5 values of initial gaps. Figure 8a about 7µm-width shows a zipping configuration resulting in a large contact area from 20µm initial gap. However, in Figure 8b for the 12µm width, the zipping configuration does not occur at 20µm and 16µm. Such an electrode width is not suitable for generating a significant force as the initial gap is of the order of 16µm and beyond.

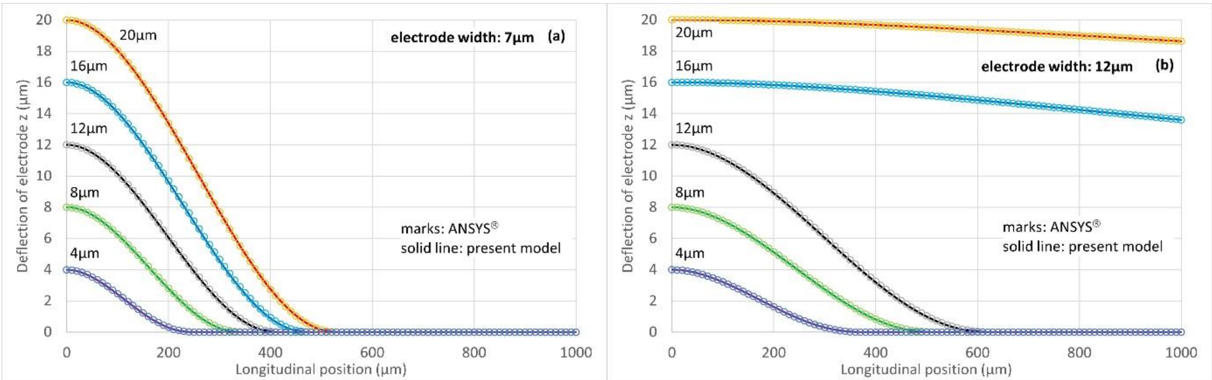

Figure 8: Deflection shapes obtained from the model and ANSYS ® results for two electrode width and five initial gap values: (a) electrode width of 7µm (b) electrode width of 12µm at 150V

About the available electrostatic force: optimum width

Figure 9 shows the evolution of the available electrostatic force for one pair of fixed/movable electrode according to three different electrode widths. In correlation with above comments, no zipping configuration (12µm wide) result in a minimum available electrostatic force close to zero within the initial 6 micrometers of travel. Moreover, mechanical performances of 7µm wide electrode are about 50% better than 4µm wide ones. For smaller width values, the force transfer is not maximized because the movable electrode is too flexible, leading to an unnecessarily large contact area. For larger width values, zipping does not occur, contact does not take place or does not propagate sufficiently, and the electrostatic force remains low similar to *ARSE*.

If this optimum value may not be realistic from a technological point of view (i.e., not feasible with MEMS technologies under consideration), the designer will have to play simultaneously on other parameters, for example increasing the length of the electrode and/or the operating voltage.

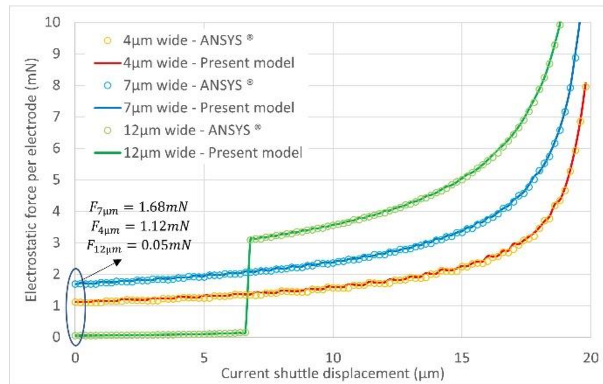

Figure 9: Available electrostatic force per electrode along a 20µm stroke at 150V, obtained from the model and ANSYS® for three electrode widths 4µm, 7µm and 12µm

Figure 9 clearly illustrates the necessity of the zipping mechanism for the actuator studied, where the stroke must accommodate a guiding system stiffness that is significant for ensuring the overall robustness of the actuator.

About the useful force: "opposable" stiffness

Determining the optimum width of the electrodes is initial consideration in sizing the guiding system and especially its "opposable" stiffness. It is important to design a guiding system that is sufficiently rigid to ensure the mechanical strength of the actuator (robustness against dynamic effects) and to make easier for the electrodes to remove. On the other hand, the maximum useful force corresponds to the minimum available electrostatic force at zero shuttle displacement (See Figure 9). As shown in Figure 10a, a maximum guiding stiffness can be designed to maintain this maximum useful force. However, it is possible to give more latitude to the design of the guiding stiffness by accepting a reduction in the useful force. Figure 10b show that guiding stiffnesses for 100%, 90%, 80% and 70% of the maximal useful force are respectively determined about 55N/m, 82N/m, 103N/m and 120N/m. According to the application, the designer will have to find a compromise between useful force and actuator robustness. It is recalled that available electrostatic and useful forces as well as guiding stiffness are defined for one single pair of fixed/movable electrode and that these characteristics are proportional to their number.

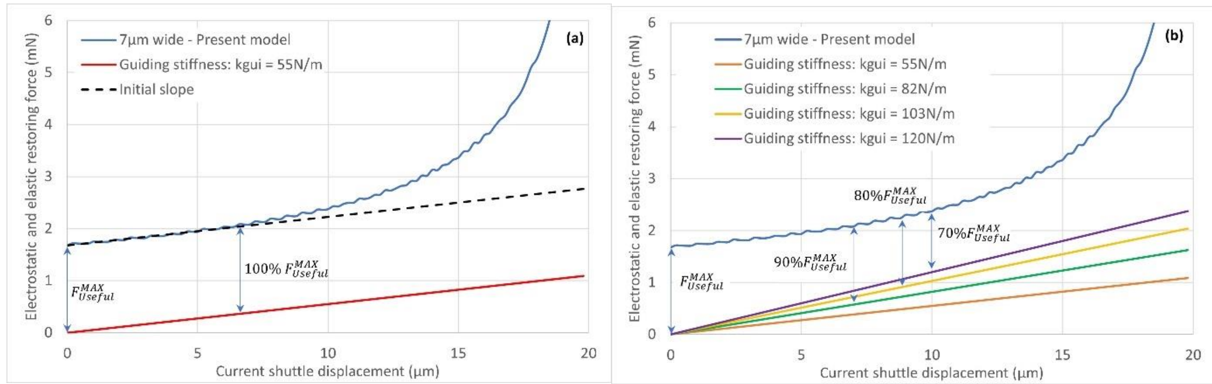

Figure 10: Useful force per electrode along a 20µm stroke at 150V versus guiding stiffness. The maximum possible useful force is identified as the minimum available electrostatic force (at $\Delta = 0$)

4. Experimental investigations: influence of the contact interface between movable and fixed electrodes on the mechanical performances of *AFSE*

4.1. Design of test devices

Experimental investigations are conducted in order to validate the model predictions in terms of available electrostatic force. In situ characterization of devices is preferred for reasons of implementation reliability, compared to the challenging coupling of a commercial sensor. Using the guiding system to discretely determine the available electrostatic force is a straightforward and practical approach. By varying the stiffness of the guiding system, specific balance points for available electrostatic forces can be achieved, where the electrostatic force is balanced with the restoring force of the guiding system. Each marker of Figure 11 represents such a balance point, and the evolution of the available electrostatic force can be approximately inferred between markers (shown as a blue dashed line). This data can then be fitted with a model simulation (blue solid line) for instance to identify parameters. It is important to note that, in this experimental context, the useful force is not addressed.

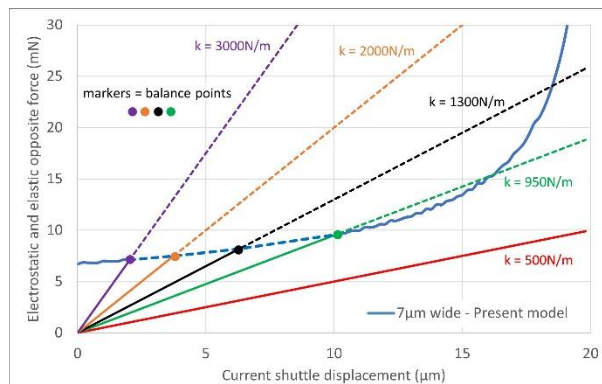

Figure 11: Using of the guiding system as a force sensor to acquire experimental "discrete" available electrostatic force for fitting with a model simulation (AFSE with 4 pair of electrodes, initial gap of 15µm, voltage of 150V)

Table 1 summarizes main parameters of the 4 set-ups studied. Figures 12 and 13 respectively show the architectures of 15µm gap set-ups and 5µm gap set-ups. For set-ups n°1/2, a vernier scale is patterned on the shuttle and a fixed part facing the shuttle (Figure 12) in order to measure the displacement to an accuracy of +/-0.5µm. For set-ups n°3/4, a displacement amplifier with a factor of around 10 (Figure 13) is added to maintain and even improve the relative accuracy with the same vernier scale. For set-ups n°3/4, the expected gap of 5µm make the actuators more sensitive to overetching. Therefore, the electrode pairs are initially patterned with a gap of 20µm and a locking system is designed to move all movable electrodes by a displacement of 15µm to obtain the expected gap of 5µm (Figure 13).

<table>
<tr><td>Specific parameters</td><td>Set-up n°1</td><td>Set-up n°2</td><td>Set-up n°3</td><td>Set-up n°4</td></tr>
<tr><td>Structural thickness (µm)</td><td>200</td><td>50</td><td>50</td><td>50</td></tr>
<tr><td>Number of pair of electrodes</td><td>12</td><td>4</td><td>8</td><td>8</td></tr>
<tr><td>Initial gap (µm)</td><td>15</td><td>15</td><td>5</td><td>5</td></tr>
<tr><td>Insulating layer material</td><td>Silicon dioxide</td><td>Silicon dioxide</td><td>Silicon dioxide</td><td>Parylene C</td></tr>
<tr><td>“sensor”: beam width (µm)</td><td>20/24/31/39</td><td>20 to 40 (by 5)</td><td>20 to 50 (by 5)</td><td>20 to 50 (by 5)</td></tr>
<tr><td>Displacement amplification</td><td>No</td><td>No</td><td>Yes</td><td>Yes</td></tr>
<tr><td>Common parameters</td><td colspan="4">Set-up n°1 – 2 – 3 – 4</td></tr>
<tr><td colspan="2">Movable electrode: length (µm) x width (µm):</td><td>1000 x 11</td><td colspan="2" rowspan="2">Insulating layer thickness (µm)
0.4</td></tr>
<tr><td colspan="2">Elastic “sensor”: beam length (µm):</td><td>1000</td></tr>
</table>

Table 1: Design features of the 4 set-ups including design values

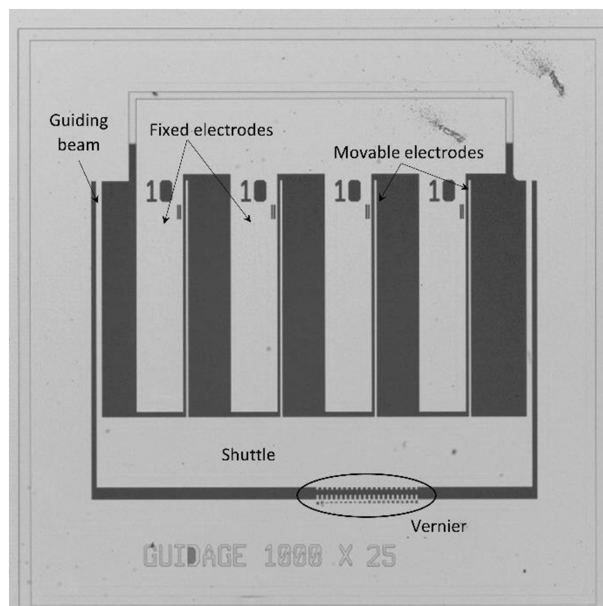

Figure 12: Microscope image of set-up n°2 (15µm gap - 4 pairs of electrodes)

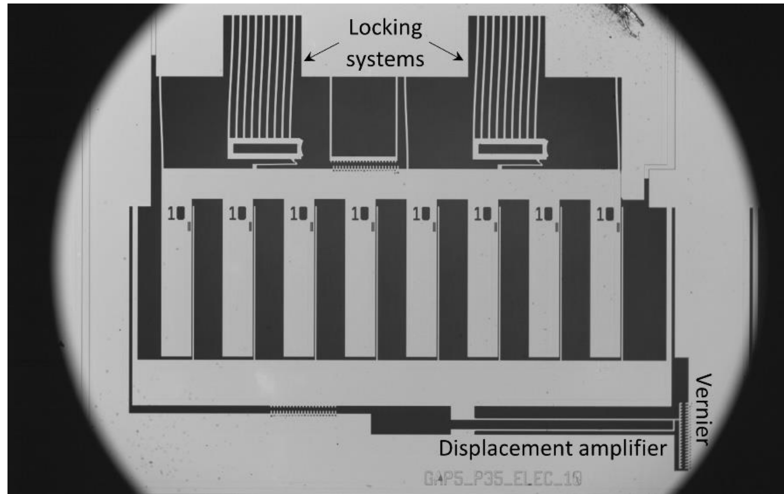

Figure 13: Microscope image of set-up n°3 (5µm gap/silicon oxide)

4.2. Fabrication and metrology

Test devices are fabricated by Deep Reaction Ion Etching of a SOI wafer according a fabrication process which the similar main steps can be found in details in [11]. For all set-ups, a double oxidation/deoxidation phase of 0.4µm is carried out to reduce and improve the roughness of the sidewalls [23]. In a very last step, an oxide layer is conformably thermally grown on set-ups n°1/2/3 and a parylene C layer is conformably deposited on set-up n°4, both 0.4µm thick. Cross-sections of movable electrodes are taken using a FIB (Focused Ion Beam) in order to qualify the deep etching process and more particularly electrode width and profile in thickness.

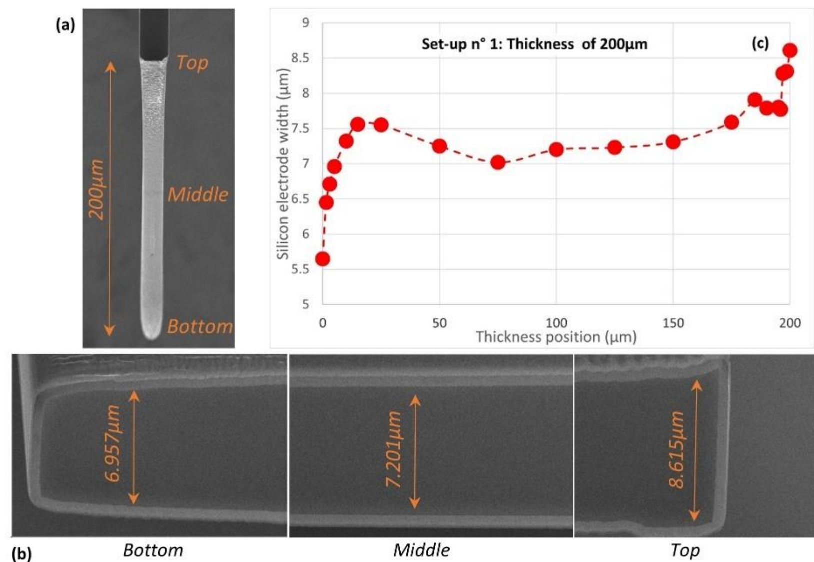

Figure 14: SEM image of electrode end (a), FIB middle cross-sections of movable electrode (b) and mean variation of electrode width along the thickness (c) in the case of 200µm thick structure (set-up n°1)

Figure 14 shows the non-verticality of sidewalls for the thickness of 200µm, with strong heterogeneity at the top just below the etch mask. There is also more over-etching at the bottom, a phenomenon

usually called “notching” [24]. In addition, electrode sides have a roughened shape more pronounced at top and bottom (See Figure 14b). This roughness, known as “scalloping”, is due to the passivation steps between each etching phase, which protect the sidewalls from lateral etching [25, 26].

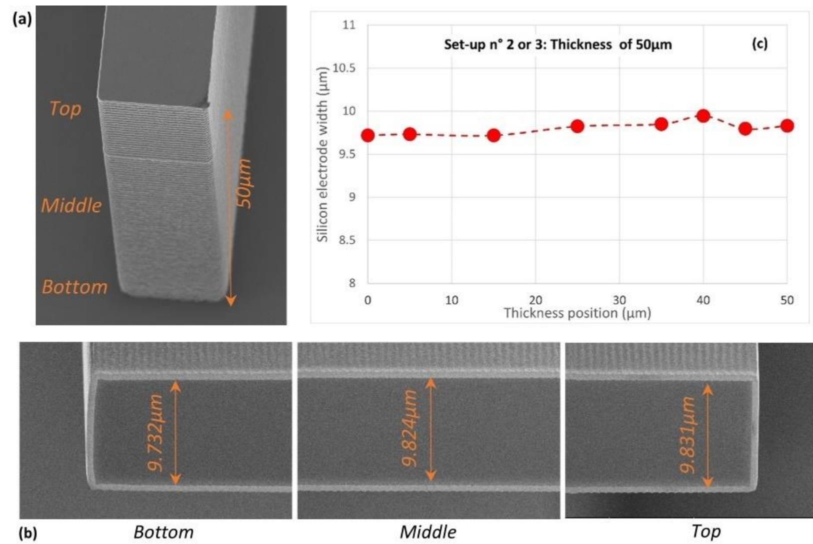

Figure 15: SEM image of electrode end (a), FIB middle cross-sections of movable electrode (b) and mean variation of electrode width along the thickness (c) in the case of 50µm thick (set-up n°2)

Figure 15 shows the very good verticality of sidewalls for the thickness of 50µm with a homogeneous width in the thickness. Similarly, roughness is more uniform than for 200µm thick structures. Deep etching of lower aspect ratio features is clearly made easier and leads to more homogeneous structures. Electrode widths initially designed at 11µm to aim at 10µm assuming an over-etching of 0.5µm per side. After fabrication, 200µm and 50µm thick electrodes are respectively 7.35µm and 9.80µm mean widths of silicon (mean of profiles described in Figures 14c and 15c). Finally, this corresponds to respective over-etching about 1.65µm and 0.075µm per side confirming the technological challenge of etching structures with a higher aspect ratio.

As the silicon electrodes are coated with silicon oxide or parylene C, “silicon equivalent” widths of bilayers are identified as inputs to the model: 7.7µm for set-up n°1 and 10.1µm for set-ups n°2/3/4. The widths of the elastic sensors (as guiding systems) and the displacement amplifier are corrected accordingly, using the same methodology.

4.3. Experimental results and discussion

All set-ups are powered by bipolar square electric signals at an actuation frequency of 1Hz, i.e., a positive voltage step is always followed by a negative one. This bipolar actuator is one of the simplest and most appropriate solutions for minimizing the electric charges trapped in the insulation layer, which could lead to irreversible stiction between movable and fixed electrodes [27]. The experimental

performance in terms of available electrostatic force is lower than the model estimates. The inability of the movable electrode to conform perfectly in thickness to the fixed electrode is highlighted as being due to the non-verticality and roughness of the sidewalls. As stated by Persano et al [5], the model, thereby, includes an additional parameter in the expression of the electrostatic pressure (Eq.2) representing a residual air thickness called h_{res} that cannot be closed:

$$p_{elec} = \frac{\varepsilon_0 \varepsilon_{ins}^2 b V^2}{2[(g_c + z(x) + \boldsymbol{h_{res}})\varepsilon_{ins} + 2h_{ins}\varepsilon_0]^2} \qquad with\ z(x) \leq 0 \tag{15}$$

Figures 16 and 17 illustrates the identification of the residual air thickness from experimental data. The solid lines represent the available electrostatic force calculated from the model for various values of residual air thickness as inputs. Experimental data points are depicted as black markers, as explained in Section 4.1 and shown in Figure 11. The dashed lines represent the restoring force, which varies linearly with the shuttle displacement. When the guiding stiffness is too low, there is no balance and the complete stroke is achieved (for example, k = 697N/m for Figure 16a). Conversely, when the guiding stiffness is sufficiently high to stop the shuttle, a balance point is reached, represented by a black marker (for example, k = 1635N/m for Figure 16a). At this balance point, the available electrostatic force equals the restoring force and can be compared to the model estimations, including a residual air thickness, for identification purposes.

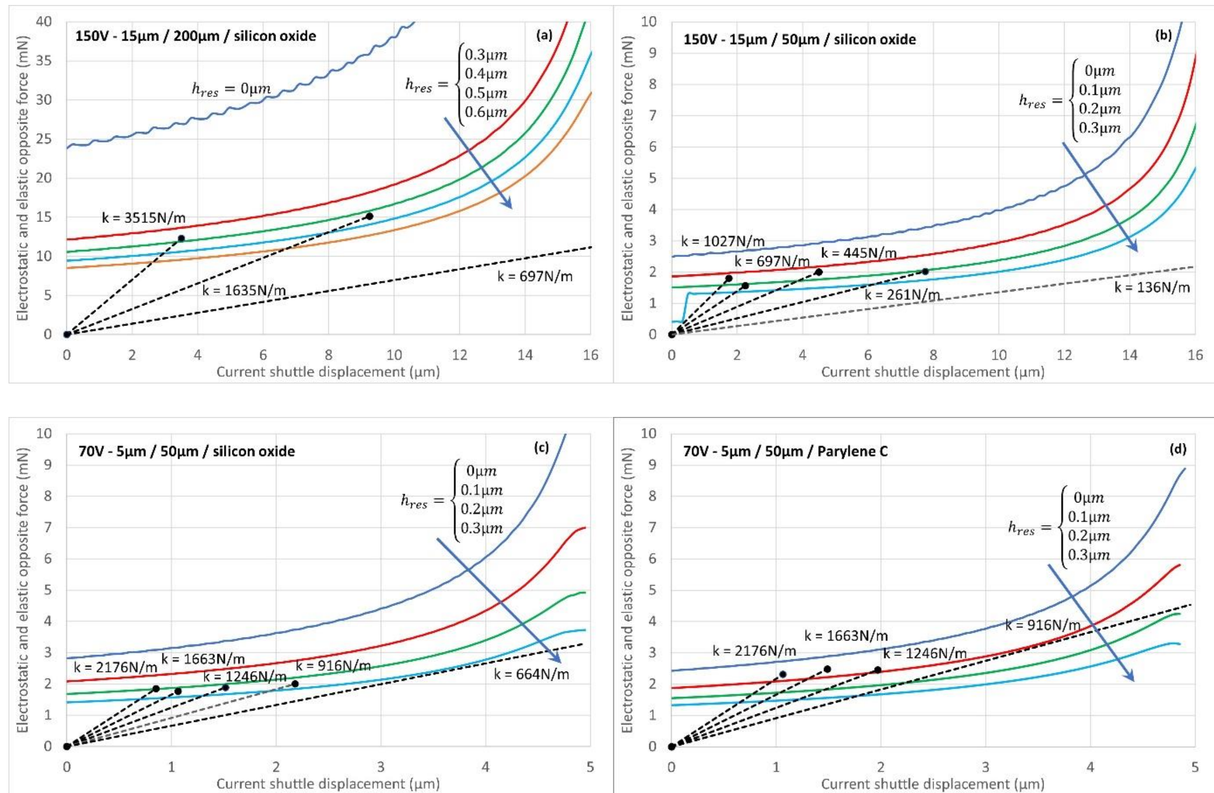

Figure 16: Identification of the residual air thickness for set-up n°1/2 (a/b) at 150V and set-up n°3/4 (c/d) at 70V

Figure 16 shows, for each of the 4 set-ups and at a given voltage, the method to estimate the order of magnitude of the residual air thickness using theoretical charts (representing different residual air thicknesses) and experimental data points. Using this methodology, Figure 17 summarizes the identification of residual air thickness throughout the entire test campaign, covering a voltage range from 40V to 200V. An amplitude identification range of 0.1 is indicated in order to take rough account of the dispersion of results. Despite this dispersion due to geometric variability, the comparison of these ranges between the set-ups is significant. The 4 set-ups, which involve various fabrication deviations, material properties and voltages, serve to highlight their respective influences on the range of residual air thickness.

Considering set-ups n°1-2 results (red and blue markers in Figure 17) respectively relative to 13.3 and 3.3 aspect ratio, improving verticality and roughness leads to lower residual air thickness: for example, at 150V, 0.35µm – 0.45µm vs 0.1µm – 0.2µm. That reflects a closer contact and thereby higher electrostatic pressure and mechanical performance.

The only difference between set-ups n°4-3 is the insulating layer material, which gives a slight smaller range of residual air thickness: 0µm – 0.2µm vs 0.1µm – 0.4µm from 50V to 110V. It highlights a closer contact with parylene C a polymer film softer than silicon oxide and as such potentially be crushed more easily.

Finally, in all graphs, it is observed that the residual air thickness decreases as voltage increases, indicating a closer contact. So, the higher the voltage, the lower the ranges tend to be. Logically, higher voltage tends to make closer the contact as shown by the trends in all the markers. This is probably caused by local bending of the flexible electrode and/or local compression of corrugation peaks.

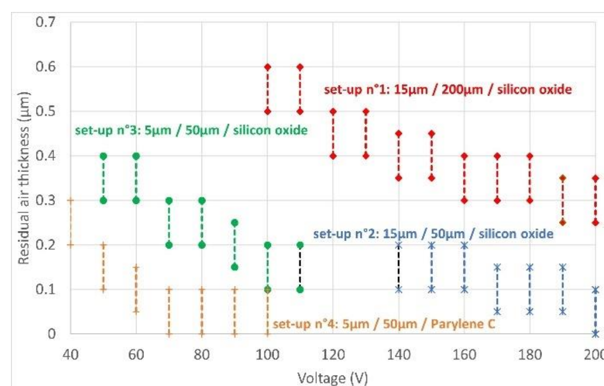

Figure 17: Identification of residual air thickness according to interface parameters

As in Figure 2, comparison of minimum calculated electrostatic force between *AFSE* and *ARIC* is again made by considering the range identified experimentally of residual air thickness 0µm – 0.6µm. Figure 18 clearly points out the influence of the residual air thickness on performance and the interest in improving the contact quality. However, the worst case (0.6µm) shows *AFSE* to be superior to *ARIC*

for any gap of less than 20µm. Thus, according to an experimental range of residual air thickness about 0µm – 0.6µm, the ratio of available electrostatic force between *AFSE* and *ARIC* is about 16.5 – 4.3, 7.3 – 2.2 and 3.1 – 1.1 for respective strokes of 5µm, 10µm and 20µm.

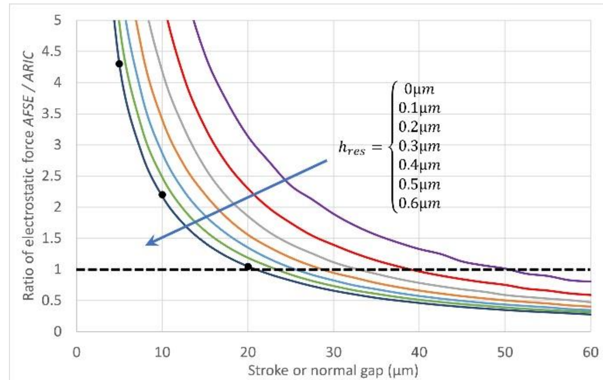

Figure 18: Ratio of electrostatic force between AFSE and ARIC – circular marks: ratios of 4.3 – 2.2 – 1.1 for h_{res} = 0.6µm

5. Conclusion

In this work, an in-depth study is carried out on understanding the electromechanical energy conversion mechanisms at the interface of actuators with flexible side-electrodes (*AFSE*). The focus is specifically on exploring the potential in terms of available electrostatic force and the useful force that can be transmitted to an external element.

An analytical model and its solution algorithm are proposed to solve the generic problem of a flexible electrode progressively contacting a fixed one under an electrostatic pressure distribution. In the case of zipping electrodes and the associated geometric ratios, the model based on the Euler-Bernoulli beam theory is highly relevant compared to ANSYS® simulations due to the simplicity with which its algorithm can be implemented in any programming language and the efficiency of its calculations. The model expresses two key features: an optimum beam width to maximize electrostatic force and the “opposable” stiffness of the guiding system, influencing the available electrostatic useful force and the useful force. Next work will aim to determine the extent to which other geometries might be affected by the edge effects neglected in this study.

Experimental component of the paper is devoted to analyze the relationship between mechanical performance and the conditions at the interface contact. The metrology campaign highlights how aspect ratio and oxidation/deoxidation procedures affect the verticality and roughness of the sidewalls. Experimental characterization including different aspect ratio, insulating layer material and operating voltages is conducted. A parameter called “residual air thickness” is introduced to consider imperfect contact between fixed and movable electrodes. Non-vertical sidewalls and roughness can

prevent the electrodes to be very close contacting. Optimum mechanical performance is accessed through a low aspect ratio and covered structures with parylene C, contributing to a reduction in residual air thickness.

An identification of the residual air thickness over the test campaign results in a range about 0µm – 0.6µm according to the contact conditions. This range impacts the corresponding ratio of electrostatic force *AFSE/ARIC* on the following values: 16.5 – 4.3, 7.3 – 2.2 and 3.1 – 1.1 for respective strokes of 5µm, 10µm and 20µm. *AFSE* becomes attractive to use, especially when the contact conditions are optimized and the stroke is small. For longer stroke actuation, concept of architectures with cumulative displacements could be envisaged by putting elementary *AFSEs* in series, each performing an elementary part of the total planned stroke.

To conclude, a design tool is proposed for *AFSE* considering technological aspects as aspect ratio, insulating layer material and voltage level. According to the applications, trade-offs must be made in balancing contradictory influences. For example, the available electrostatic force and the useful force are proportional to the structural thickness, however higher structural thickness results in higher aspect ratio involving potential sidewalls defects. Likewise, a softer insulating layer as parylene C is relevant from a contact aspect, but that could lead to wear limitations. More generally, improving the contact between fixed and movable electrodes can benefit to the mechanical performances but stiction problems could be amplified and become redhibitory. Finally, this work will need to be continued to investigate dynamic limitations and long-term behavior. Regarding dynamic effects, this could involve considering the influence of bending modes of movable flexible electrodes and rigid body modes of the shuttle on the maximum actuation frequency. Additionally, it is well-known that reliability and durability are common concerns for actuators involving contact, such as switches. Therefore, tests over a large number of cycles will need to be conducted to validate that the actuators continue to operate correctly over the long term. If not, optimum conditions in terms of actuation frequency and shapes of electric signals should be identified in relation to optimum mechanical designs.

Acknowledgements: The microfabrication of devices was performed at Center of Microtechnology (CMI) at EPFL, Lausanne, Switzerland with the support of the CMI-staff. The metrology and characterization were supported by the French RENATECH network and its FEMTO-ST technological facility.

Bibliography:

[1] W. Niu, L. Fang, L. Xu, X. Li, R. Huo, D. Guo, Z. Qi, "Summary of Research Status and Application of MEMS accelerometers", Journal of Computer and Computations, 6, 215-221, 2018.
https://doi.org/10.4236/jcc.2018.612021

[2] E.E. Moreira, B. Kuhlmann, F.S. Alves, R.A. Dias, J. Cabral, J. Gaspar, L.A. Rocha, "Highly sensitive MEMS frequency modulated accelerometer with small footprint", Sensors and Actuators A: Physical, Vol. 307, 2020, 112005.
https://doi.org/10.1016/j.sna.2020.112005

[3] M. Imboden, J. Chang, C. Pollock, E. Lowell, M. Akbulut, J. Morrison, T. Stark, D.J. Bishop, "High-Speed Control of Electromechanical Transduction: Advanced Drive Techniques for Optimized Step-and-Settle Response of MEMS Micromirrors", IEEE Control Systems Magazine, Vol. 36, Issue: 5, 48-76, October 2016.
https://doi.org/10.1109/MCS.2016.2584338

[4] F. Ceyssens, S. Sadeghpour, H. Fujita, R. Puers, "Actuators: Accomplishments, opportunities and challenges", Sensors and Actuators A: Physical, Vol. 295, 2019, 604-611
https://doi.org/10.1016/j.sna.2019.05.048

[5] A. Persano, F. Quaranta, M.C. Martucci, P. Siciliano, A. Cola, "On the electrostatic actuation of capacitive RF MEMS switches on GaAs substrate", Sensors and Actuators A: Physical, Vol. 232, 2015, 202-207.
https://doi.org/10.1016/j.sna.2015.05.008

[6] J.J. Percy, S. Kanthamani, "Revolutionizing wireless communication: A review perspective on design and optimization of RF MEMS switches", Microelectronics Journal, Vol. 139, 2023, 105891.
https://doi.org/10.1016/j.mejo.2023.105891

[7] H. Saleh, M. Shojaeian, R. Bajwa, I. Tekin, M.K. Yapici, "Low actuation voltage cantilever-type RF-MEMS shunt switches for 5G applications", Microelectronics Reliability, Vol. 136, 2022,114645.
https://doi.org/10.1016/j.microrel.2022.114645

[8] R. Wierzbicki, C. Adda, H. Hotzendorfer, "Electrostatic Silicon Microgripper with Low Voltage of Actuation", 2007 International Symposium on Micro-NanoMechatronics and Human Science, November 2007, 344-349.
https://doi.org/10.1109/MHS.2007.4420878

[9] S.A. Bazaz, F. Khan, R. I. Shakoor, "Design, simulation and testing of electrostatic SOI MUMPs based microgripper integrated with capacitive contact sensor", Sensors and Actuators A: Physical, Vol. 167, Issue 1, 2011, 44-53
https://doi.org/10.1016/j.sna.2010.12.003

[10] D. Sadhukhan, G.P. Singh, "Design of electrostatic actuated MEMS biaxial scanning micro-mirror with serpentine structure", Materialstoday: Proceedings, Vol. 65, Part 1, 2022, 229-234
https://doi.org/10.1016/j.matpr.2022.06.120

[11] K. Laszczyk, S. Bargiel, C. Gorecki, J. Krezel, P. Dziuban, M. Kujawinska, D. Callet, S. Frank, "A two directional electrostatic comb-drive X-Y micro-stage for MOEMS applications", Sensors and Actuators A: Physical, Vol. 163, Issue 1, 2010, 255-265
https://doi.org/10.1016/j.sna.2010.06.020

[12] H. Ameur, P. Le Moal, G. Bourbon, C. Vuillemin, M. Sworowski, "Suppressing residual vibrations in comb-drive electrostatic actuators: A command shaping technique adapted to nomadic applications", Sensors and Actuators A: Physical, Vol. 334, 2022, 113366
https://doi.org/10.1016/j.sna.2022.113366

[13] P.H. Pham, D.V. Dao, L.B. Dang, S. Sugiyama, "Single mask, simple structure micro rotational motor driven by electrostatic comb-drive actuators", Journal of Micromechancis and Microengineering, 22, 2012, 015008
http://dx.doi.org/10.1088/0960-1317/22/1/015008

[14] I. Penskiy, S. Bergbreiter, "Optimized electrostatic inchworm motors using a flexible driving arm", Journal of Micromechanics and Microengineering, Vol. 23, Number 1, 2013, 015018
http://doi.org/10.1088/0960-1317/23/1/015018

[15] D. Teal, H.C. Gomez, C.B. Schindler, K.S.J. Pister, "Robust Electrostatic Inchworm Motors for Macroscopic Manipulation and Movement", 21st International Conference on Solid-State Sensors, Actuators and Microsystems (Transducers), 20-24 June 2021, Orlando, USA
https://doi.org/10.1109/Transducers50396.2021.9495446

[16] M. Bao, "Analysis and Design Principles of MEMS Devices", Elsevier Science, 2005, ISBN 978-0-444-51616-9,
https://doi.org/10.1016/B978-0-444-51616-9.X5000-0

[17] R. Legtenberg, J. Gilbert, S.D. Senturia, M. Elwenspoek, "Electrostatic curved electrode actuators", Journal of Microelectromechanical Systems, V. 6, Issue 3, 1997, 257-265
https://doi.org/10.1109/84.623115

[18] J. Li, M.P. Brenner, T. Christen, M.S. Kotilainen, J.H. Lang, A.H. Slocum, "Deep-reactive ion-etched compliant starting zone electrostatic zipping actuators", Journal of Microelectromechanical Systems, Vol. 14, Issue 6, December 2005, 1283-1297
https://doi.org/10.1109/JMEMS.2005.851842

[19] S.P. Burugupally, "Mechanics of a curved electrode actuator operating in viscous dielectric media: simulation and experiment", Journal of Micro-Bio Robotics, Vol. 15, 2019, 43-51
https://doi.org/10.1007/s12213-019-00114-2

[20] M. Hoffmann, D. Nûsse, E. Voges, "Electrostatic parallel-plate actuators with large deflections for use in optical moving-fibre switches", Journal of Micromechanics and Microengineering, Vol. 11, Number 4, 2001, 323-328
http://doi.org/10.1088/0960-1317/11/4/306

[21] J. Li, "Electrostatic zipping actuators and their applications to MEMS", Ph.D. dissertation, Massachusetts Institute of Technology, Cambridge, MA, USA, 2004
https://dspace.mit.edu/handle/1721.1/33678

[22] J. Oberhammer, A.Q. Liu, G. Stemme, "Time-Efficient Quasi-Static Algorithm for Simulation of Complex Single-Sided Clamped Electrostatic Actuators", Journal of Microelectromechanical Systems, Vol. 16, Issue 2, 2007, 373-382
https://doi.org/10.1109/JMEMS.2007.892917

[23] T.M. Fahim Amin, "Design and Fabrication of Micro-electro-mechanical Systems Actuators for Application in External Cavity Tunable Lasers", Ph.D. dissertation, Department of Electrical and Computer Engineering, University of Alberta, USA, 2014
https://doi.org/10.7939/R3VT1GV7N

[24] M. Huff, "Recent advances in Reactive Ion Etching and Applications of High-Aspect-Ratio Microfabrication", Micromachines, 12 (8), 991, 2021
https://doi.org/10.3390/mi12080991

[25] R. Abdolvand, F. Ayazi, "An advanced reactive ion etching process for very high aspect-ratio sub-micron wide trenches in silicon", Sensors and Actuators A, Vol. 144, Issue 1, 109-116, 2008
https://doi.org/10.1016/j.sna.2007.12.026

[26] Z.A. Syed Mohammed, M.A.S. Olimpo, D.P. Poenar, S. Aditya, "Smoothening of scalloped DRIE trench walls", Materials Science in Semiconductor Processing", 63, 83-89, 2017.
https://doi.org/10.1016/j.mssp.2017.02.006

[27] Z. Peng, X. Yuan, J.C.M. Hwang, D.I. Forehand, "Dielectric Charging of RF MEMS Capacitive Switches under Bipolar Control-Voltage Waveforms", 2007 IEEE/MTTS-S International Microwave Symposium, 03-08 June 2007, Honolulu, HI, USA.
https://doi.org/10.1109/MWSYM.2007.380102

APPENDIX

1. Calculation of $M_{elec}(x)$ in Eq. (8), F_{tot} and M_{tot} in Eq. (6)

$$M_{elec}(x) = \int_{x}^{x_{j+1}} p_j(u)(u-x)du + \sum_{k=j+1}^{k=n} \int_{x_k}^{x_{k+1}} p_k(u)(u-x)du \tag{A.1}$$

with:

$$\int_{x}^{x_{j+1}} p_j(u)(u-x)du = \frac{(p_{j+1}-p_j)}{(x_{j+1}-x_j)}\left(\frac{x_{j+1}^3}{3}+\frac{x^3}{6}-\frac{x x_{j+1}^2}{2}-\frac{x_j x_{j+1}^2}{2}-\frac{x_j x^2}{2}+x x_j x_{j+1}\right)+p_j\frac{(x_{j+1}-x)^2}{2}$$

$$\int_{x_k}^{x_{k+1}} p_k(u)(u-x)du$$
$$= p_k\left(\frac{x_{k+1}^2}{2}-\frac{x_k^2}{2}-x(x_{k+1}-x_k)\right)+\frac{(p_{k+1}-p_k)}{(x_{k+1}-x_k)}\left(\frac{x_{k+1}^3}{3}+\frac{x_k^3}{6}-\frac{x x_{k+1}^2}{2}-\frac{x_k x_{k+1}^2}{2}-\frac{x x_k^2}{2}+x x_k x_{k+1}\right)$$

$$\begin{cases} F_{tot} = \int_0^L p(x)dx = \sum_{j=1}^{j=n} \frac{(p_{j+1}+p_j)}{2}(x_{j+1}-x_j) \\ M_{tot} = \int_0^L p(x)x dx = \sum_{j=1}^{j=n} \frac{(x_{j+1}-x_j)}{6}\left[p_{j+1}(2x_{j+1}+x_j)+p_j(x_{j+1}+2x_j)\right] \end{cases} \tag{A.2}$$

2. *Analytical expressions of $U_j(x)$ and $T_j(x)$ in Eq. (9)*

$$\begin{cases} \tilde{F}_j(x) = -\dfrac{(p_{j+1}-p_j)}{(x_{j+1}-x_j)}\left(\dfrac{x_{j+1}^3 x}{3}+\dfrac{x^4}{24}-\dfrac{x^2 x_{j+1}^2}{4}-\dfrac{x_j x_{j+1}^2 x}{2}-\dfrac{x_j x^3}{6}+\dfrac{x^2 x_j x_{j+1}}{2}\right) \\ \qquad +p_j\dfrac{(x_{j+1}-x)^3}{6} \\ F_k(x) = \dfrac{(p_{k+1}-p_k)}{(x_{k+1}-x_k)}\left(\dfrac{x_{k+1}^3 x}{3}+\dfrac{x_k^3 x}{6}-\dfrac{x^2 x_{k+1}^2}{4}-\dfrac{x_k x_{k+1}^2 x}{2}-\dfrac{x^2 x_k^2}{4}+\dfrac{x^2 x_k x_{k+1}}{2}\right) \\ \qquad +p_k\left(\dfrac{x_{k+1}^2 x}{2}-\dfrac{x_k^2 x}{2}-\dfrac{x^2}{2}(x_{k+1}-x_k)\right) \end{cases} \tag{A.3}$$

$$\begin{cases} \tilde{G}_j(x) = -\dfrac{(p_{j+1}-p_j)}{(x_{j+1}-x_j)}\left(\dfrac{x_{j+1}^3 x^2}{6}+\dfrac{x^5}{120}-\dfrac{x^3 x_{j+1}^2}{12}-\dfrac{x_j x_{j+1}^2 x^2}{4}-\dfrac{x_j x^4}{24}+\dfrac{x^3 x_j x_{j+1}}{6}\right) \\ \qquad -p_j\dfrac{(x_{j+1}-x)^4}{24} \\ G_k(x) = \dfrac{(p_{k+1}-p_k)}{(x_{k+1}-x_k)}\left(\dfrac{x_{k+1}^3 x^2}{6}+\dfrac{x_k^3 x^2}{12}-\dfrac{x^3 x_{k+1}^2}{12}-\dfrac{x_k x_{k+1}^2 x^2}{4}-\dfrac{x^3 x_k^2}{12}+\dfrac{x^3 x_k x_{k+1}}{6}\right) \\ \qquad +p_k\left(\dfrac{x_{k+1}^2 x^2}{4}-\dfrac{x_k^2 x^2}{4}-\dfrac{x^3}{6}(x_{k+1}-x_k)\right) \end{cases} \tag{A.4}$$

$$\begin{cases} U_n(x) = \tilde{G}_n(x) \quad if\ x \in [x_n, x_{n+1}]\ (j=n) \\ U_j(x) = \tilde{G}_j(x) - \displaystyle\sum_{k=j+1}^{k=n} G_k(x) \quad if\ x \in [x_j, x_{j+1}]\ (j \in \{1,\dots,n-1\}) \end{cases} \tag{A.5}$$

$$\begin{cases} T_n(x) = \tilde{F}_n(x) \quad if\ x \in [x_n, x_{n+1}]\ (j=n) \\ T_j(x) = \tilde{F}_j(x) - \displaystyle\sum_{k=j+1}^{k=n} F_k(x) \quad if\ x \in [x_j, x_{j+1}]\ (j \in \{1,\dots,n-1\}) \end{cases} \tag{A.6}$$

3. *Analytical expressions of AF_j* **and** AG_j *in Eq. (12)*

For $j \in \{1,2,\dots,n-1\}$

$$\begin{cases} AF_j = \dfrac{1}{EI}\left(\tilde{F}_j(x_{j+1}) - \tilde{F}_{j+1}(x_{j+1}) - \displaystyle\sum_{k=j+1}^{k=n} F_k(x_{j+1}) + \sum_{k=j+2}^{k=n} F_k(x_{j+1})\right) \\ AG_j = \dfrac{1}{EI}\left(\tilde{G}_j(x_{j+1}) - \tilde{G}_{j+1}(x_{j+1}) - \displaystyle\sum_{k=j+1}^{k=n} G_k(x_{j+1}) + \sum_{k=j+2}^{k=n} G_k(x_{j+1})\right) \end{cases} \tag{A.7}$$